

# Interplay of magnetization dynamics with microwave waveguide at cryogenic temperatures

I. A. Golovchanskiy<sup>1,2</sup>, N. N. Abramov<sup>2</sup>, M. Pfirrmann<sup>3</sup>, T. Piskor<sup>3</sup>, J. N. Voss<sup>3</sup>,  
 D. S. Baranov<sup>1,4,5</sup>, R. A. Hovhannisyan<sup>1</sup>, V. S. Stolyarov<sup>1,4,6</sup>, C. Dub<sup>7</sup>,  
 A. A. Golubov<sup>1,8</sup>, V. V. Ryazanov<sup>2,4,6</sup>, A. V. Ustinov<sup>2,3</sup>, M. Weides<sup>3,9</sup>

<sup>1</sup> *Moscow Institute of Physics and Technology, State University,*

<sup>9</sup> *Institutskiy per., Dolgoprudny, Moscow Region, 141700, Russia*

<sup>2</sup> *National University of Science and Technology MISIS, 4 Leninsky prosp., Moscow, 119049, Russia*

<sup>3</sup> *Physikalisches Institut, Karlsruhe Institute of Technology, 76131 Karlsruhe, Germany*

<sup>4</sup> *Institute of Solid State Physics (ISSP RAS), Chernogolovka, Moscow Region 142432, Russia*

<sup>5</sup> *Laboratoire de Physique et d'Etude des Matériaux, UMR8213,*

*École supérieure de physique et de chimie industrielles de la Ville de Paris, Paris Sciences et Lettres Research University, Institut des NanoSciences de Paris-Sorbonne Université, 10 rue Vauquelin, 75005 Paris, France*

<sup>6</sup> *Solid State Physics Department, Kazan Federal University, Kazan 420008, Russia*

<sup>7</sup> *INNOVENT e.V. Technologieentwicklung, Pruessingstrasse 27B, 07745 Jena, Germany*

<sup>8</sup> *Faculty of Science and Technology and MESA+ Institute for Nanotechnology, University of Twente, Enschede 7500 AE, The Netherlands*

<sup>9</sup> *School of Engineering, University of Glasgow, Rankine Building, Oakfield Avenue, Glasgow G12 8LT, United Kingdom*

In this work, magnetization dynamics is studied at low temperatures in a hybrid system that consists of thin epitaxial magnetic film coupled with superconducting planar microwave waveguide. The resonance spectrum was observed in a wide magnetic field range, including low fields below the saturation magnetization and both polarities. Analysis of the spectrum via a developed fitting routine allowed to derive all magnetic parameters of the film at cryogenic temperatures, to detect waveguide-induced uniaxial magnetic anisotropies of the first and the second order, and to uncover a minor misalignment of magnetic field. A substantial influence of the superconducting critical state on resonance spectrum is observed and discussed.

## I. INTRODUCTION

The field of magnonics study application of magnetization oscillations and waves in ferromagnetic structures<sup>1–6</sup>. The following benefits make magnonics promising for application in processing of microwave signals: tunability of the magnon dispersion by applied magnetic field and geometry of a media, low dissipation, low power consumption and high operation frequencies, convenient micro- and sub-micro-scales of spin wavelength at microwave frequencies, and, finally, absence of parasitic coupling of spin waves with nonmagnetic environment. Conventionally, magnonics is a room-temperature research discipline.

Currently a sub-discipline emerges that can be referred to as “cryogenic magnonics”. Indeed, on one hand, quantum magnonics is of high current interest<sup>7–11</sup>. Microwave experiments in quantum magnonics are typically performed at milli-kelvin temperatures and often using setups equipped with superconducting quantum circuits. On the other hand, a development of various hybrid devices takes place based on superconducting resonators<sup>7,12</sup> and Josephson junctions<sup>13–15</sup>. Also, it was shown that hybridization of a magnon media with passive superconducting structures result in substantial modification of dispersion properties<sup>16–19</sup>. At last, metamaterial properties have been reported for superconductor/ferromagnet superlattices<sup>20</sup>. More general, and beyond superconductor-induced phenomena, the magnetic

properties at low temperatures are probed in absence, or only with minor, thermal excitations. Typical thermal effects for standard magnonics, such as reduced saturation magnetization or thermally activated domain wall motion, are lessened for cryo-magnonics, leading to new phenomena in ferromagnetic resonance (FMR).

In this regard, investigation of magnetic properties of ferromagnetic films at low temperature as well as of their interaction with superconducting circuits is imperative. This report address both problems. We focus on the ferromagnetic resonance in a thin Yttrium Iron Garnet (YIG) film coupled to a superconducting Nb planar waveguide at out-of-plane magnetic field. We obtain the FMR spectrum at low temperature in a wide field range. The spectrum shows linear magnetic resonance versus field dependence for high fields, and a range of nonlinear dependence of FMR frequency on field at low magnetic fields where the Kittel formulas are inapplicable. Developing a fitting routine we derive all magnetic parameters of the YIG film. Our analysis shows that the waveguide itself induces substantial uniaxial magnetic anisotropy. Next, we study the FMR spectrum at temperatures below superconducting critical temperature of the waveguide and observe an influence of the superconducting critical state of Nb on the resonance spectrum.

We note that while YIG is probably the most popular magnetic materials for magnonic applications owing to its essentially low damping, the damping in YIG and its temperature dependence are not addressed in this paper

and can be found elsewhere<sup>21–23</sup>. In this report, YIG is selected as a model magnetic single-crystalline thin film with distinct magnetocrystalline anisotropy and sufficiently low saturation magnetization, which is convenient for out-of-plane measurements.

## II. EXPERIMENTAL DETAILS

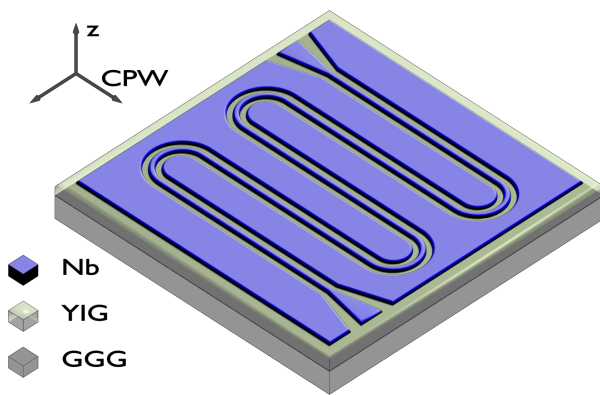


FIG. 1. Schematic illustration of the investigated system. YIG epitaxial film is grown on [111]-oriented single-crystal GGG substrate by means of LPE. A Nb CPW is fabricated directly on top of YIG film. The main direction of the CPW is indicated with the axis. Magnetic field  $H$  is applied out-of-plane, along [111] orientation of YIG/GGG (i.e., along  $z$ -direction).

The FMR absorption measurements were performed using the so-called VNA-FMR approach<sup>24–26</sup> (VNA stands for the vector network analyzer). A schematic illustration of the investigated system is shown in Fig. 1. The single-crystalline epitaxial YIG film of thickness  $d = 51$  nm was deposited on single-crystal [111]-oriented Gadolinium Gallium Garnet (GGG) substrate using the liquid phase epitaxy (LPE) technique. Details of LPE as well as room-temperature characteristics of LPE-grown ultra-thin YIG films can be found elsewhere<sup>22,27</sup>. The FMR response in YIG was enabled by fabrication of coplanar waveguide (CPW) directly on top of YIG film. CPW was patterned out of 150 nm thick magnetron sputtered niobium (Nb) thin film with superconducting critical temperature  $T_c \simeq 8.5$  K using photo-lithography and plasma-chemical etching. Deposition of Nb at room temperature was obstructed by poor adhesion of metal film to YIG surface, and, thereby, was performed at 300°C. The 50  $\Omega$  impedance of superconducting CPW was provided by 27-40-27  $\mu\text{m}$  gap-center-gap dimensions. Direct placement of CPW on probed ferromagnetic films and its elongation via meandering enhance sensitivity to weak FMR absorptions<sup>28</sup>. The experimental chip was installed in a copper sample holder and wire bonded to PCB with RF connectors. A thermometer and a heater were attached directly to the holder for precise temperature control.

The holder was placed in a superconducting solenoid inside a closed-cycle cryostat (Oxford Instruments Triton, base temperature 1.2 K). The response of the system was studied by analyzing the transmitted microwave signal  $S_{21}$  with the VNA Rohde & Schwarz ZVB20.

## III. RESULTS AND DISCUSSION

Figure 2a,b shows transmission spectra of the studied sample at  $T = 10$  K  $> T_c$  and  $2$  K  $< T_c$  of Nb. Spectra have been normalized with  $S_{21}(f)$  at  $\mu_0 H = 0.5$  T. Figure 2c,d shows a set of normalized absorption curves  $S_{21}(f)$  of the sample at the same temperatures and several magnetic fields. Field dependent spectral lines in Fig. 2a,b with the minimum transmission correspond to FMR curves  $f_r(\mu_0 H)$ . Both spectra show linear FMR response at  $|\mu_0 H| > 0.2$  T, which is typical for the Kittel-FMR mode of a thin film at out-of-plane magnetic field. The resonance frequency at out-of-plane field is  $f_r \propto (\mu_0 H - 4\pi M_{eff})$ , that indicates the value of the effective saturation magnetization  $4\pi M_{eff} \sim 2000$  Oe at  $f_r \rightarrow 0$ . Upon decreasing  $|\mu_0 H|$  the linear resonance line is terminated with a kink at  $|\mu_0 H| \sim 4\pi M_{eff}$  and transforms into two FMR branches with nonlinear dependence of resonance frequency versus field for  $|\mu_0 H| < 4\pi M_{eff}$ . We refer to the higher-frequency FMR branch with stronger absorption as C-line and to the lower-frequency FMR branch with weaker absorption as G-line. At out-of-plane field  $|\mu_0 H| < 4\pi M_{eff}$  ferromagnetic films are not magnetized to saturation and Kittel formulas for FMR are not applicable. Split of FMR response into several spectral lines at  $|\mu_0 H| < 4\pi M_{eff}$  can be justified by various factors, including standing spin wave resonances<sup>18,29–31</sup>, FMR response of magnetic domain structure<sup>32–34</sup>, or magnetic phase separation.

After transition into superconducting state of Nb CPW the transmission spectrum changes (compare Fig. 2a and b, Fig. 2c and d). While the spectrum at  $T < T_c$  consists of the same resonance lines as at  $T > T_c$ , superconductivity manifests itself in hysteresis of FMR peak absorption at  $|\mu_0 H| < 0.2$  T, which is the best visible for C-line (compare  $S_{21}(f)$  at  $\mu_0 H = 0.1$  T and  $\mu_0 H = -0.1$  T in Fig. 2d): FMR absorption at negatively swept magnetic field (positive  $H$  in Fig. 2b,d) is substantially stronger than at positively swept magnetic field (negative  $H$  in Fig. 2b,d). In addition, at  $T < T_c$  a suppression of FMR response is observed at low field region  $|\mu_0 H| < 0.02$  T.

Note, that in general observation of FMR in thin films at out-of-plane geometry at  $|\mu_0 H| < 4\pi M_{eff}$  might be challenging due to formation of nonuniform magnetization configurations. Also, to our best knowledge, spectra in Fig. 2 are the first continuous observation of FMR at the out-of-plane geometry at the field range  $0 \leq |\mu_0 H| < 4\pi M_{eff}$ . Below we will discuss FMR response of YIG in absence of superconductivity, establish causes for the split of FMR at  $|\mu_0 H| < 4\pi M_{eff}$ , and define contribution of superconductivity to FMR spectrum.

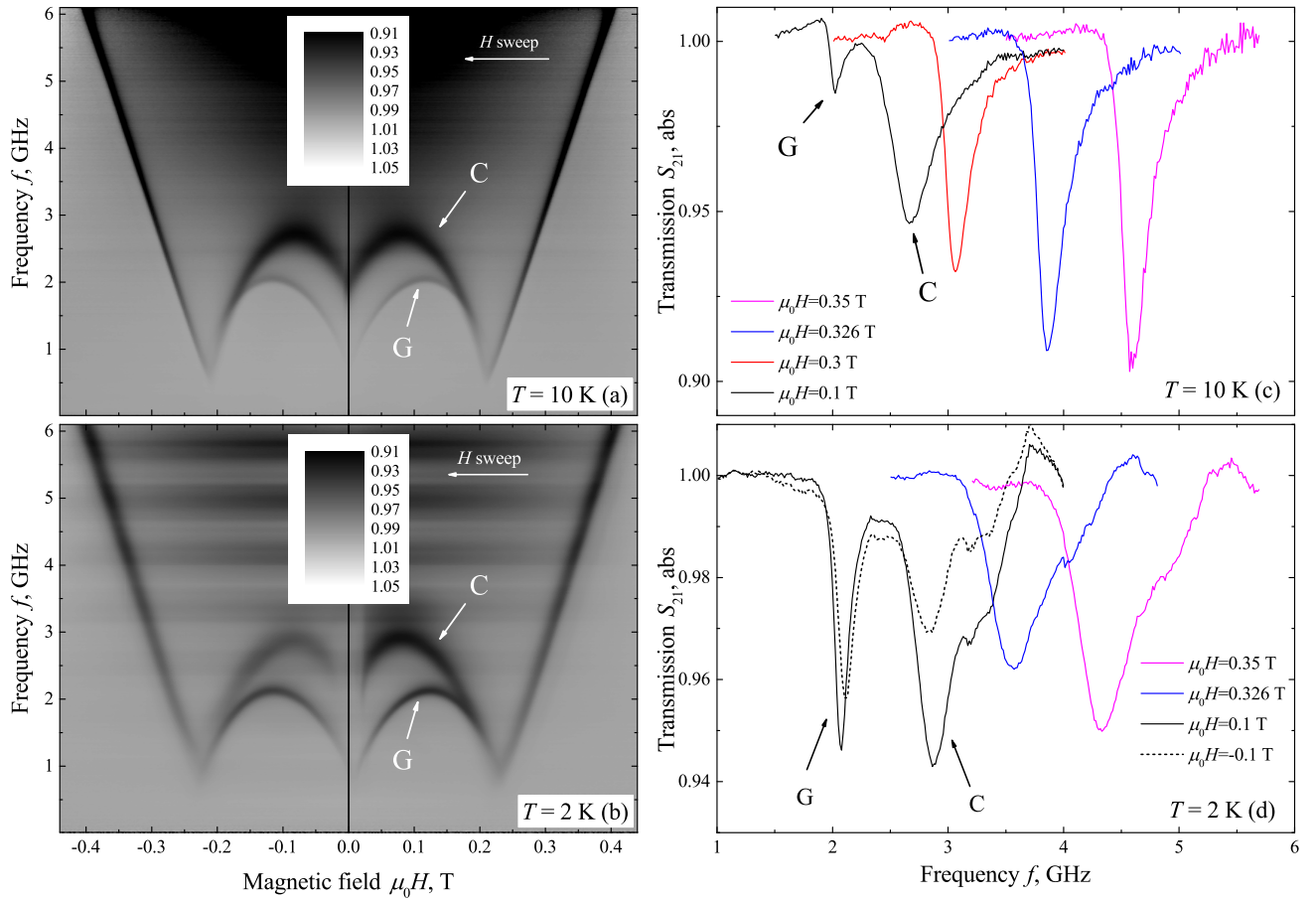


FIG. 2. a) and b) Gray-scale-coded transmission spectra  $|S_{21}(\mu_0 H, f)/S_{21}(\mu_0 H = 0.5 \text{ T}, f)|$  measured at  $T = 10 \text{ K}$  above  $T_c$  (a) and  $T = 2 \text{ K}$  below  $T_c$  (b). c) and d) Corresponding frequency dependencies of the normalized transmission  $|S_{21}(f)|$  at several magnetic fields at  $T = 10 \text{ K}$  above  $T_c$  (c) and  $T = 2 \text{ K}$  below  $T_c$  (d). For curves in (c) and (d) the background was subtracted. At  $T < T_c$  the spectrum shows hysteresis of absorption. Magnetic field was swept negatively from  $+0.5$  to  $-0.5 \text{ T}$  (indicated with arrows), and, therefore, the part of spectra in (b) at positive fields provides the “down-field-sweep” data while the part of the spectrum at negative fields provides the “up-field-sweep” data. C and G indicate higher- and lower-frequency spectral lines, respectively.

### A. FMR at $T > T_c$ . Magnetic properties of YIG film at cryogenic temperatures.

After analysis of possible origins for FMR split into C-line and G-line in Fig. 2 we can state that neither domain structure nor spin waves can contribute into FMR spectrum for our particular study. For instance, nucleation of magnetic domains upon demagnetization at  $\mu_0 H < 4\pi M_{eff}$  occurs for thin films with strong perpendicular anisotropy in comparison with the demagnetizing energy<sup>35,36</sup>, i.e. when the magnetic quality parameter  $Q = K_u/2\pi M_s^2 > 1$ , where  $K_u$  is the out-of-plane uniaxial anisotropy, and  $M_s$  is the saturation magnetization. However, typical field of uniaxial anisotropy  $\mu_0 H_{K_u} = 2K_u/M_s$  in LPE-grown YIG thin films ranges up to  $\sim 200 \text{ Oe}$ <sup>22,27,31,37</sup> ensuring  $Q \ll 1$ . The highest values of uniaxial anisotropy in YIG films  $\mu_0 H_{K_u} \sim 10^3 \text{ Oe}$  can be obtained in pulsed-laser-deposited films<sup>38</sup>

still ensure  $Q < 1$ . As an additional test we have performed a magnetic force microscopy study of magnetic flux structure at the surface of YIG film at 4 K using attocube attoDRY 1000 closed-cycle cryogenic microscope, supplied with a superconducting solenoid, and found no traces of domains or any field-dependent magnetic structure. Therefore, we confirm that formation of domain structure does not occur. Magnetic state of YIG film is single-domain, variation of the out-of-plane component of magnetization at  $\mu_0 H < 4\pi M_{eff}$  occurs via rotation of magnetization vector from out-of-plane orientation to in-plane.

The absence of contribution of standing spin wave resonances into FMR spectrum can be illustrated in the following way. At  $H = 0$  magnetization vector of a single-domain film is aligned in-plane. Therefore, the Kittel formula for FMR and dispersion relations for any spin wave mode at  $H = 0$  become applicable. When several

resonances are observed a contributing spin wave mode can be identified by estimating a resonance frequency difference  $\Delta f_r$  between the Kittel mode and any standing spin wave resonance mode. The latter appears due to quantization of the wavelength with geometrical parameters of a sample. The difference  $\Delta f_r$  is then compared with the experimentally observed one  $\sim 1.3$  GHz at  $H = 0$  (Fig. 2). If an in-plane magnetostatic standing spin wave mode<sup>39,40</sup> is assumed, i.e., backward volume mode or magnetostatic surface mode, its wavelength  $\lambda/2$  for standing mode should be quantized with scales of CPW, i.e.,  $\lambda/2 \sim 20 - 40 \mu\text{m}$ . Such standing spin wave mode provides only marginal difference  $\Delta f_r \lesssim 10$  MHz due to small ratio  $d/\lambda \sim 10^{-3}$ . Alternatively, if exchange-dominated perpendicular standing spin wave resonance<sup>41,42</sup> is assumed the typical exchange constant in YIG films<sup>31</sup>  $\sim 4 \times 10^{-12} \text{ J/m}$  provides  $\Delta f_r \sim 2.5$  GHz for  $d = \lambda/4$  and  $\Delta f_r \sim 7.5$  GHz for  $d = \lambda/2$ . Thus, none of possible standing spin wave modes can provide  $\Delta f_r \sim 1.3$  GHz. Overall, when a standing spin wave resonance is excited multiple consequential spectral lines are expected. FMR absorption for each line should decrease progressively with the mode number (see, for instance Ref.<sup>43</sup>). Such picture is not observed in our experiment. Therefore, we confirm that several spectral lines in Fig. 2 at  $|\mu_0 H| < 4\pi M_s$  are not caused by standing spin wave modes.

The remaining explanation for two FMR lines requires the existence of two resonating areas with different magnetic properties in vicinity of CPW. The magnetic structure essentially is single-domain in each area. The resonating areas can be identified by the coupling strength of microwaves to precessing magnetization that is proportional to the FMR amplitude and correlates directly to the amplitude of excitation AC magnetic fields. In CPW geometry AC magnetic fields are mainly focused in vicinity to the central transmission line<sup>12,24</sup>. Therefore, geometry of the experiment (Fig. 1) suggests that the lower-frequency weaker G-line originates from YIG at gap areas of CPW where the coupling is weaker, while higher-frequency stronger C-line appears due to FMR response of YIG area under the central conducting line of the CPW. The accuracy of that explanation is strengthened by additional features, as discussed below.

For the case of single-domain single-crystalline YIG film analytical resonance curve  $f_r(\mu_0 H)$  can be obtained in the entire  $H$ -range following Refs.<sup>44–46</sup> (we keep notations given in Ref.<sup>37</sup>). Orientation of magnetization of a single-domain film at arbitrary oriented magnetic field is defined by the minimum of free magnetostatic energy  $g = g(M_s, h, k_1, k_2, k_u, \theta, \psi, \phi_h, \phi_m)$ , where  $k_1$ ,  $k_2$  and  $k_u$  are unitless parameters of cubic magnetocrystalline anisotropy and out-of-plane uniaxial anisotropy, respectively,  $h = \mu_0 H/4\pi M_s$  is the normalized external magnetic field, and  $\theta, \psi, \phi_h, \phi_m$  define orientation of  $H$  and  $M_s$  in respect to principle crystallographic axes of YIG in spherical coordinates (see Fig. 3). In addition, the system in Fig. 1 has a distinct directionality along ori-

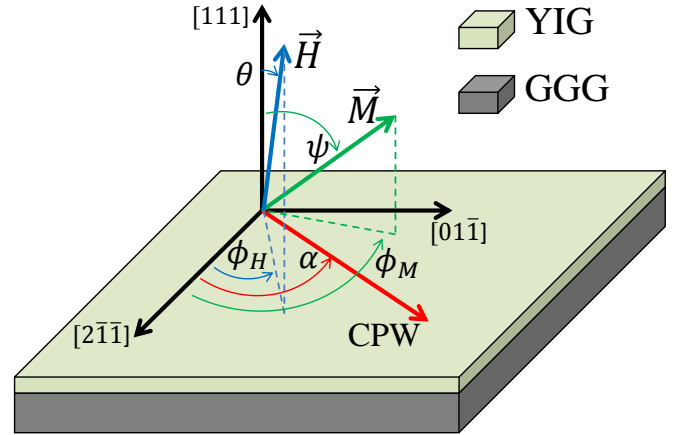


FIG. 3. Spherical coordinate system for the studied YIG film sample. Adopted from Ref.<sup>37</sup>. Direction of the CPW transmission line (see Fig. 1) is indicated with the red axis, which specifies additional in-plane uniaxial anisotropy due to CPW directionality .

tation of CPW. This directionality may contribute into orientation of magnetization. We account its possible contribution by additional energy term  $g_a$  added to the free magnetostatic energy  $g$  that provides a phenomenological in-plane uniaxial anisotropy of the first order. The term of the in-plane uniaxial anisotropy of the first order in coordinates of Fig. 3 is

$$g_a = -k_{a1} \sin(\psi)^2 \cos(\phi_h - \alpha)^2. \quad (1)$$

FMR frequency is defined by derivatives at position of minimum of free energy<sup>44–46</sup> as

$$f_r \sim \gamma(g_{\psi\psi}g_{\phi_m\phi_m} - g_{\psi\phi_m}^2)^{1/2} / \sin(\psi) \quad (2)$$

where  $\gamma$  is the gyromagnetic ratio. See Refs.<sup>37,44–46</sup> for details.

Dotted data in Fig. 4 show the experimental  $f_r(\mu_0 H)$  resonance curves extracted from Fig. 2a. First, we focus on the G-line of FMR spectrum. In order to fit the data we have developed the following routine, which allowed us to obtain all magnetic parameters of  $g$  and  $f_r$ , despite a large number of parameters and their partial interdependency. First, we note that when misalignment of orientation of magnetic field with the z-axis  $\theta$  is small, and in-plane CPW uniaxial anisotropy  $k_{a1}$  is negligible, the linear part at  $\mu_0 H \gg 4\pi M_{eff}$  can be fitted with the simplified expression<sup>37</sup>

$$f_r = 2\gamma M_s(h - (1 - k_u + 2k_1/3 + 2k_2/9)) \quad (3)$$

Fitting the data in the field range from 0.3 T to 0.4 T with Eq. 3 we obtain the gyromagnetic ratio  $\gamma/2\pi = 2.985$  GHz/kOe, which is close to the ratio for a free electron 2.803 GHz/kOe, and also the value of saturation magnetization in relation with anisotropy parameters  $4\pi M_{eff} = 4\pi M_s \times (1 - k_u + 2k_1/3 + 2k_2/9) = 1975$  Oe.

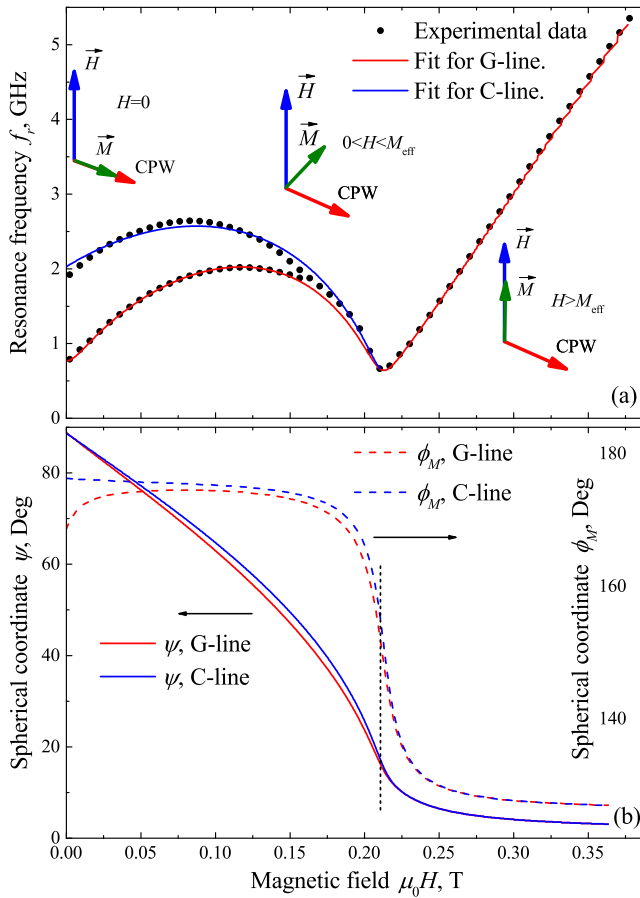


FIG. 4. Fitting experimental  $f_r(\mu_0 H)$ . (a) Dependence of FMR frequencies of magnetic field. CPW induces 1st (G-line) and 2nd order (C-line) uniaxial anisotropy. Pictograms in (a) illustrate orientation of magnetization relative to orientations of magnetic field and CPW axis at different magnetic fields. (b) Dependence of free-energy-minimum orientations of magnetization on magnetic field. Dotted line indicates position of the kink in FMR curves.

Next we note that (i) the position of the kink at  $\mu_0 H \simeq 0.22$  T on  $(f_r, \mu_0 H)$  plot is mostly determined by misalignment of the magnetic field with z-axis, i.e., by  $\theta$  and  $\phi_H$ ; (ii) the position of the maximum of FMR frequency at  $\mu_0 H \simeq 0.12$  T on  $(f_r, \mu_0 H)$  plot is mostly determined by parameters of magnetocrystalline anisotropy  $k_1$  and  $k_2$ ; (iii) knowing  $\theta$ ,  $\phi_H$ ,  $k_1$  and  $k_2$  the slope of the resonance curve  $f_r(\mu_0 H)$  at  $H \rightarrow 0$  and the value  $f_r(H = 0)$  are defined by the CPW-induced uniaxial anisotropy, i.e., by  $k_{a1}$  and  $\alpha$  in Eq. 1. Using least-squares method for optimization through steps from (i) to (iii) and back, after several runs (iv) the fit is further optimized by adjusting parameter  $k_u$ . Following the routine (i)-(iv) we have obtained a optimum fit of G-line (see red curve in Fig. 4a) with the following parameters:  $4\pi M_s = 1876$  Oe,  $k_1 = -0.16$ ,  $k_2 = 0.18$ ,  $k_u = -0.12$ ,  $\theta = 1.4$ ,  $\phi_h = 126^\circ$ ,  $k_{a1} = 0.025$ ,  $\alpha = 177^\circ$ . Importantly, parameters of

the cubic magnetocrystalline anisotropy  $k_1$  and  $k_2$  are by a factor of 2-3 higher than typical values at room temperature<sup>22,37</sup>. This trend correlates well with the temperature dependence of the cubic magnetocrystalline anisotropy in YIG bulk single crystals<sup>47</sup>.

After fitting the G-line, that correspond to FMR response of YIG areas at CPW gaps, we state that the only option to fit C-line, that correspond to FMR response of YIG areas under the central CPW line, is by introducing additional term into energy  $g$  that represent the second order uniaxial anisotropy induced by CPW. The term of the in-plane uniaxial anisotropy of the second order in coordinates of Fig. 3 is

$$g_a = -(k_{a1} + 2k_{a2}) \sin(\psi)^2 \cos(\phi_h - \alpha)^2 + k_{a2} \sin(\psi)^4 \cos(\phi_h - \alpha)^4 \quad (4)$$

Using magnetic parameters obtained for the G-line the fitting procedure for the C-line with the anisotropy given by Eq. 4 provides  $k_{a1} = 0.121$  and  $k_{a2} = -0.048$ . This fit is shown in Fig. 4a with blue curve.

Possible origins of the CPW-induced anisotropy include a distinct directionality of microwave currents. Also, directionality of surface stress can be considered that appear due to differences in thermal expansion of narrow central transmission line of metal CPW and YIG/GGG oxides. Surface stress may appear either due to deposition of Nb film at elevated temperature or due to performance of experiments at cryogenic temperatures. For instance, the difference in thermal expansions between Nb and garnets can enable a strain in YIG at 2 K of up to  $\epsilon \approx +6 \times 10^{-4}$  along the CPW in case of absence of mechanical relaxation in Nb. In contrast, if a complete relaxation of tensions occurs in Nb at the room temperature the difference in thermal expansions enables the opposite-sign strain in YIG of  $\epsilon \approx -4 \times 10^{-4}$ . Both values of the strain are well comparable with the growth induced tensions, provided by the lattice misfit between the GGG substrate and YIG film, that induce the uniaxial anisotropy in LPE-grown<sup>27</sup> and PLD-grown films<sup>48,49</sup>. See the Appendix section for details. Importantly, presence of both first- and second-order anisotropies suggests different mechanisms for their induction.

Figure 4b shows dependencies of orientations of magnetization  $\psi(\mu_0 H)$  and  $\phi_M(\mu_0 H)$  for C- and G-lines of FMR spectrum on magnetic field. A marginal difference between C- and G-curves at the entire field range indicates co-alignment of magnetization orientations at both gap and center areas of CPW, implying that the entire volume of YIG subjected to FMR remains at the single-domain state throughout the experiment.

Our experimental setup does not allow us to study microwave transmission of at higher temperatures  $T \gtrsim 15$  K. Thereby, temperature dependence of magnetic parameters of YIG is not addressed in this report and can be found elsewhere<sup>21,22,50</sup>.

## B. FMR at $T < T_c$ . Impact of the superconducting critical state.

At  $T < T_c$  of Nb, in presence of superconductivity, FMR absorption spectrum changes (see Fig. 2b). Since the Nb CPW is placed directly on YIG film, all changes in absorptions of C-branch can be attributed to magnetization state under the Nb line, that can be discussed in terms of the superconducting critical state. Therefore, the effect of superconductivity on FMR can be tracked by analyzing the superconducting critical state of Nb film and its variation with applied magnetic field.

Figure 5a shows the zero-field-cooled (ZFC) transmission spectra that is acquired when the sample is cooled down to 2 K at zero magnetic field, and then  $S_{21}$  measurements were performed sweeping magnetic field from 0 to 0.11 T. Figure 5b shows the field-cooled (FC) transmission spectra that is acquired when the sample was cooled down to 2 K at  $\mu_0 H = 0.25$  T, and then  $S_{21}$  measurements were performed sweeping magnetic field back from 0.11 T down to 0. The hysteresis in peak absorption can be tracked by fitting  $S_{21}(f)$  curves at each value of  $H$  and plotting dependencies of FMR amplitude on magnetic field  $I(\mu_0 H)$  (Fig. 5c).  $I(\mu_0 H)$  curves correspond to variation of the coupling strength of FMR to CPW with magnetic field, which correlates with homogeneity of magnetization and magnetic flux distribution in YIG induced by Nb line in superconducting critical state.

First, we focus on the ZFC curve in Fig. 5c where three parts can be distinguished. At the first part of the curve, the strongest FMR absorption is observed with  $I \sim 0.1$  at narrow interval of low fields  $0 \leq \mu_0 H \lesssim 2 \times 10^{-3}$  T (highlighted with a red circle in Fig. 5a). This corresponds to the Meissner state of Nb line when Meissner screening currents circulate at the edges of Nb film and exclude magnetic flux from its cross-section. At the Meissner state DC magnetic flux remains homogeneous across Nb line that ensures a strong coupling of CPW to YIG at FMR. At the second part, at  $2 \times 10^{-3} < \mu_0 H < 10^{-2}$  T FMR absorption drops rapidly from  $I \sim 0.1$  to the minimum  $I \sim 0.02$ . This drop can be explained by transition into the partially penetrated superconducting critical state when superconducting vortices start to penetrate Nb film. At partial penetration the magnetic flux profile in superconducting films is the most inhomogeneous<sup>51-53</sup> which cause a weak coupling of FMR to CPW and low absorption intensity. The partial penetration state commences at the first critical field of superconducting film  $\mu_0 H_{c1} \sim 2 \times 10^{-3}$  T where first vortices start to penetrate into the film, taking into account its demagnetizing factor, and terminates with the magnetic field of full penetration 0.01 T. At the third part of ZFC curve, at  $\mu_0 H > 0.01$  T, after full penetration is reached, magnetic flux in superconducting film forms a constant gradient that can be depicted by the Bean critical state model<sup>54-57</sup>. The gradient is formed due to pinning of vortices and induces a homogeneous circulating critical currents. Upon increasing magnetic field pin-

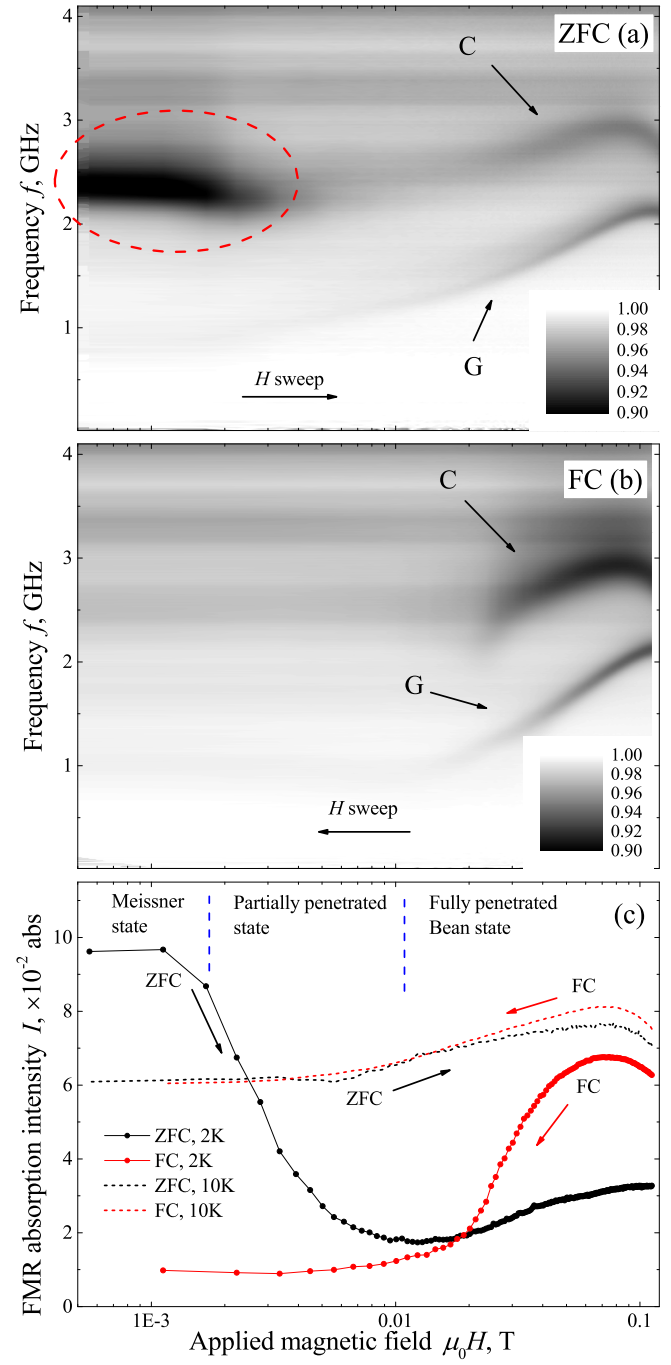


FIG. 5. Gray-scale-coded transmission spectra  $|S_{21}(\mu_0 H, f)/S_{21}(\mu_0 H = 0.5 \text{ T}, f)|$  measured at 2 K starting from ZFC state (a) and FC state (b). C and G spectral lines are indicated. Red circle in (a) highlights FMR absorption at the Meissner state of CPW. c) Dependencies of resonance peak absorption for C-lines on magnetic field  $I(\mu_0 H)$  obtained at 2 K and 10 K. Direction of magnetic field sweep is indicated with arrows. The  $\mu_0 H$  axis is given on log scale. Field regions for three superconducting states of Nb at ZFC curve in (c) are separated with blue dashed lines.

ning of vortices reduces and the slope of magnetic flux also reduces<sup>56,57</sup> making magnetic flux in YIG more homogenous. Smaller gradient of magnetic flux in superconductor increases the coupling that we observe in gradual increase of FMR peak absorption upon increasing magnetic field from 0.01 T to higher fields. Note, that such a nonmonotonic behavior of  $I(\mu_0 H)$  is not observed for the G-line (Fig. 5a), which evidences additionally that absorption at G-line is caused by FMR at the gap areas of CPW where influence of the superconducting state of Nb is marginal.

Increasing magnetic field further beyond the field range in Fig. 5 the ZFC curve should coincide with the FC curve at the so-called irreversibility field<sup>57-59</sup> where pinning of vortices becomes negligible. At field ranges in Fig. 5 the FC curve consist of two parts. At the first part at  $\mu_0 H > 0.03$  T the coupling remains by a factor of  $\sim 2$  higher than for ZFC curve. This happens because upon decreasing magnetic field the Bean critical currents counter-act the Meissner currents, diamagnetic response of superconducting film is reduced as compared to ZFC curve measured at sweeping up  $H$ <sup>59</sup>, and influence on YIG at FMR decreases. At the second part, upon decreasing magnetic field at  $0 < \mu_0 H < 0.03$  T  $I$  drops rapidly which can be explained by a gradual formation of a complex remanent critical state at  $H = 0$  with highly nonuniformly distributed frozen magnetic flux. Also at low magnetic field magnetization of individual vortices may contribute into inhomogeneity of magnetization of YIG by inducing high local magnetic fields up to  $\mu_0 H_v \sim \Phi_0/\pi\lambda_L^2 \sim 0.06$  T, where  $\Phi_0$  is the magnetic flux quantum and  $\lambda_L \sim 10^{-7}$  m is the typical London penetration depth in Nb films.

Overall, influence of the superconducting critical state in our geometry on FMR seems to be destructive. FMR intensity for both ZFC and FC curves remains below values of  $I$  at  $T > T_c$  (Fig. 5c). However, magnetic hysteresis often is employed in magnetic logic devices. Also, in vicinity to  $H = 0$  FMR is substantially stronger when superconductor is in the Meissner state than for normal metal CPW. This effect may be a result of interaction of magnetic moments in YIG with Meissner screening currents in the ideal diamagnet.

#### IV. CONCLUSION

In conclusion, ferromagnetic resonance of YIG is studied at out-of-plane magnetic fields and cryogenic temperatures using a superconducting coplanar waveguide fabricated directly on top of magnetic film (see Fig. 1). FMR absorption spectra are obtained in a wide field range. Nonlinear dependence of FMR frequency on magnetic field at low magnetic field, below the field of saturation magnetization, showed a split of resonance into two spectral lines which were identified as FMR response of YIG at gap areas of CPW and of YIG located directly under the central conducting line of CPW.

A special routine was developed for fitting FMR spectra. This routine allowed us to obtain all magnetic parameters of YIG, i.e., the saturation magnetization, the gyromagnetic ratio, and parameters of magnetocrystalline and out-of-plane uniaxial anisotropies. In addition, the fitting routine have issued the misalignment angle of 1.4° between magnetic field and the out-of-plane orientation, and parameters of in-plane magnetic anisotropy of first and second order which are induced by the CPW.

FMR spectrum at temperatures below superconducting critical temperature of the waveguide showed a hysteresis in FMR peak absorption. The hysteresis is explained by influence of magnetization of Nb transmission line at the superconducting critical state. Tracking the dependence of the intensity of FMR on magnetic field allowed us to identify all fundamental states of a superconducting film at out-of-plane magnetic field, i.e., the Meissner state, the partially penetrated state and the fully penetrated Bean critical state. Also, it allowed to justify the hysteresis by pinning of magnetic vortices which induces the gradient of magnetic flux in superconducting films. The gradient is controlled by direction of magnetic field sweep.

In general, this report suggests that development of magnonics at cryogenic temperatures may be beneficial due to: (i) substantially different properties of magnetic materials, including magneto-crystalline anisotropy, (ii) possibility to engineer additional anisotropies with metal structures, and (iii) potential to affect the spectra by hybridization of a magnonic media with superconductors.

*Note added.* While we were preparing the manuscript, a related work by Jeon et al. on effect of the superconducting critical state on magnetization dynamics in thick superconductor/ferromagnet/superconductor trilayers appeared<sup>60</sup>.

#### V. ACKNOWLEDGMENTS

Authors acknowledge Lucas Radtke and Yannick Schoen for assistance with sample preparation and measurements. This work was supported by the European Research Council (ERC) under the Grant Agreement 648011, Deutsche Forschungsgemeinschaft (DFG) within Project INST 121384/138-1 FUGG. C.D. thanks the Deutsche Forschungsgemeinschaft for financial support under contract number DFG DU 1427/2-1. I.A.G. acknowledges support by the German Academic Exchange Service (DAAD) via the program “Research Stays for University Academics and Scientists 2017”. I.A.G., N.N.A., V.V.R., and A.V.U. acknowledge the Ministry of Education and Science of the Russian Federation (Research Project K2-2018-015 in the framework of the Increase Competitiveness Program of NUST MISiS) for support in microwave measurements. V.S.S., I.A.G., D.S.B. and A.A.G. acknowledge the joint Russian-Greek projects RFMEFI61717X0001 and T4DPX-00031 Exper-

imental and theoretical studies of physical properties of low-dimensional quantum nanoelectronic systems for support in numerical analysis and MFM investigations.

## VI. APPENDIX: STRESS INDUCED IN YIG BY NB CPW

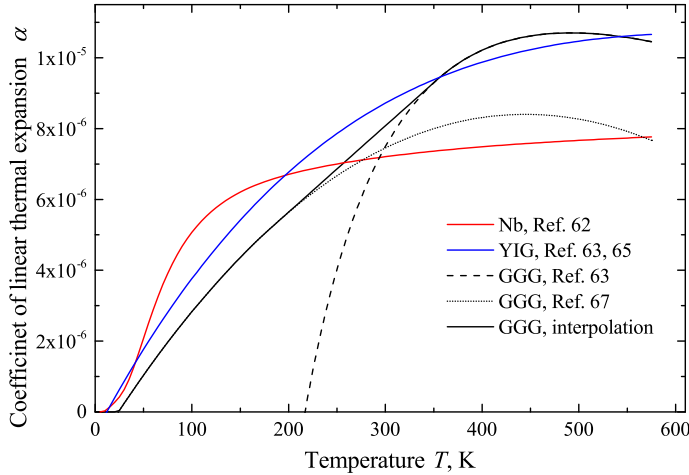


FIG. 6. Dependencies of the thermal expansion coefficient on temperature  $\alpha(T)$  for Nb, YIG and GGG.

One of possible causes of the CPW induced anisotropy that is derived in Sec. IIIA is the stress in YIG that is forced by differences in thermal expansion of narrow extended central transmission line of metal CPW and YIG/GGG oxides. Assuming that during deposition of Nb at the deposition temperature  $T_d \approx 600$  K an unstressed continuous interface is formed between Nb and YIG the stress at the interface at measurement temperature  $T_m = 2$  K can be estimated with the following expression

$$\sigma \approx \frac{E}{1-\nu} \epsilon = \frac{E}{1-\nu} \int_{T_d}^{T_m} [\alpha_G(T) - \alpha_{Nb}(T)] dT. \quad (5)$$

where  $\sigma$  is the stress in YIG,  $E = 2 \times 10^{12}$  dyne/cm<sup>2</sup> is the Young's modulus of YIG at the temperature range from 0 to 300 K<sup>61</sup>,  $\nu = 0.29$  is the Poisson's ratio,  $\epsilon$  is the strain at the interface at  $T_m$  due to the difference in

thermal expansion,  $\alpha_G(T)$  and  $\alpha_{Nb}(T)$  are temperature dependencies of the linear thermal expansion of the garnet and Nb, respectively. Importantly, the stress in Eq. 5 implies absence of mechanical relaxation.

However, estimation of the stress at the Nb/YIG interface using Eq. 5 is impeded. While thermo-mechanical properties of Nb are well studied in a wide temperature range<sup>62</sup> from  $\approx 0$  K up to about the melting point, a consistent study of thermo-mechanical properties of YIG is not available for the required temperature range. The coefficient  $\alpha_G(T)$  for YIG is available piecewise and can be obtained by interpolation of  $\alpha_G(T)$  at temperatures above<sup>63,64</sup> and below<sup>65</sup> the room temperature. On the other side, the coefficient  $\alpha_G(T)$  for YIG can be substituted with one for GGG since their thermo-mechanical properties are almost identical<sup>63,64</sup>. The coefficient  $\alpha_G(T)$  for GGG is reported for several temperature ranges separately: room temperature and higher temperatures data is available in Refs.<sup>63,64</sup>,  $\alpha_G(T)$  at low temperatures is reported in Ref.<sup>66</sup> for the range from 6 K to 300 K and in Ref.<sup>67</sup> for the range from 80 K to 330 K.

Figure 6 shows dependencies of the thermal expansion on temperature  $\alpha(T)$ . Red curve shows  $\alpha_{Nb}(T)$  for Nb that is calculated using Ref.<sup>62</sup>. Blue curve shows  $\alpha_G(T)$  for YIG that is calculated using Refs.<sup>63,65</sup>. Black dashed and dotted curves show  $\alpha_G(T)$  for GGG that are calculated using Ref.<sup>63</sup> and Ref.<sup>67</sup>, respectively. Solid black curve shows linear interpolation between lower-temperature and higher-temperature curves  $\alpha_G(T)$  for GGG at the range from 180 K up to 330 K. The interpolated dependence  $\alpha_G(T)$  is used for calculations.

Calculations with Eq. 5 and coefficients  $\alpha(T)$  in Fig. 6 provide the strain at YIG/Nb interface  $\epsilon \approx +6.4 \times 10^{-4}$  that produces the compressive stress  $\sigma \sim 10^9$  dyne/cm<sup>2</sup>. Note however, that if the room-temperature deposition of Nb takes place, or the strain in Nb relaxes at room temperature, according to Eq. 5 and Fig. 6 an opposite-sign strain  $\epsilon \approx -4 \times 10^{-5}$  emerges at cryogenic temperature  $T_m$ . If the data for GGG is used instead of YIG, the integral in Eq. 5 provides approximately the same strain  $\epsilon \approx +5.6 \times 10^{-4}$  at the interface with unrelaxed Nb, and a larger opposite-sign strain  $\epsilon \approx -4 \times 10^{-4}$  at the interface with the room-T deposited or relaxed Nb. These values are well comparable with the growth induced tensions, provided by the lattice miss-fit between the GGG substrate and YIG film, that induce the uniaxial anisotropy in LPE-grown<sup>27</sup> and PLD-grown<sup>48,49</sup> films.

<sup>1</sup> B. Lenk, H. Ulrichs, F. Garbs, and M. Münzenberg, Phys. Rep. **507**, 107 (2011).

<sup>2</sup> A. V. Chumak, V. I. Vasyuchka, A. A. Serga, and B. Hillebrands, Nat. Phys. **11**, 453 (2015).

<sup>3</sup> Y. Kajiwara, K. Harii, S. Takahashi, J. Ohe, K. Uchida, M. Mizuguchi, H. Umezawa, H. Kawai, K. Ando, K. Takanashi, et al., Nature **464**, 262 (2010).

<sup>4</sup> Special Issue on Magnonics, J. Phys. D: Appl. Phys. **50** (2017).

<sup>5</sup> S. O. Demokritov and A. N. Slavin, eds., *Magnonics: From Fundamentals to Applications* (Springer-Verlag Berlin Heidelberg, 2013).

<sup>6</sup> M. Evelt, L. Soumah, A. Rinkevich, S. Demokritov, A. Anane, V. Cros, J. B. Youssef, G. de Loubens, O. Klein,

P. Bortolotti, et al., *Phys. Rev. Appl.* **10**, 041002 (2018).

<sup>7</sup> H. Huebl, C. W. Zollitsch, J. Lotze, F. Hocke, M. Greifenstein, A. Marx, R. Gross, and S. T. B. Goennenwein, *Phys. Rev. Lett.* **111**, 127003 (2013).

<sup>8</sup> Y. Tabuchi, S. Ishino, T. Ishikawa, R. Yamazaki, K. Usami, and Y. Nakamura, *Phys. Rev. Lett.* **113**, 083603 (2014).

<sup>9</sup> X. Zhang, C.-L. Zou, L. Jiang, and H. X. Tang, *Phys. Rev. Lett.* **113**, 156401 (2014).

<sup>10</sup> R. G. E. Morris, A. F. van Loo, S. Kosen, and A. D. Karenowska, *Sci. Rep.* **7**, 11511 (2017).

<sup>11</sup> M. Pfirrmann, I. Boventer, M. Klaeui, A. V. Ustinov, and M. Weides, in preparation (2018).

<sup>12</sup> I. A. Golovchanskiy, N. N. Abramov, V. S. Stolyarov, I. V. Shchetinin, P. S. Dzhumaev, A. S. Averkin, S. N. Kozlov, A. A. Golubov, V. V. Ryazanov, and A. V. Ustinov, *J. Appl. Phys.* **123**, 173904 (2018).

<sup>13</sup> S. E. Barnes, M. Aprili, I. Petkovic, and S. Maekawa, *Supercond. Sci. Technol.* **24**, 024020 (2011).

<sup>14</sup> S. Mai, E. Kandelaki, A. F. Volkov, and K. B. Efetov, *Phys. Rev. B* **84**, 144519 (2011).

<sup>15</sup> I. A. Golovchanskiy, N. N. Abramov, V. S. Stolyarov, O. V. Emelyanova, A. A. Golubov, A. V. Ustinov, and V. V. Ryazanov, *Supercond. Sci. Technol.* **30**, 054005 (2017).

<sup>16</sup> B. Lebed and S. Yzkovlev, *Pis'ma v ZhTF* **15**, 27 (1989).

<sup>17</sup> A. Vashkovskiy, V. Zubkov, and E. Lokk, *Fizika Tverdogo Tela* **39**, 2195 (1997).

<sup>18</sup> I. A. Golovchanskiy, N. N. Abramov, V. S. Stolyarov, V. V. Bolginov, V. V. Ryazanov, A. A. Golubov, and A. V. Ustinov, *Adv. Func. Mater.* **28**, 1802375 (2018).

<sup>19</sup> I. A. Golovchanskiy, N. N. Abramov, V. S. Stolyarov, V. V. Ryazanov, A. A. Golubov, and A. V. Ustinov, *J. Appl. Phys.* **124**, 233903 (2018).

<sup>20</sup> A. Pimenov, A. Loidl, P. Przyslupski, and B. Dabrowski, *Phys. Rev. Lett.* **95**, 247009 (2005).

<sup>21</sup> M. Haidar, M. Ranjbar, M. Balinsky, R. K. Dumas, S. Khartsev, and J. Akerman, *J. Appl. Phys.* **117**, 17D119 (2015).

<sup>22</sup> N. Beaulieu, N. Kervarec, N. Thiery, O. Klein, V. Naletoff, H. Hurdequin, G. de Loubens, J. B. Youssef, and N. Vukadinovic, *IEEE Magnetics Letters* **9**, 3706005 (2018).

<sup>23</sup> I. Boventer, M. Pfirrmann, J. Krause, Y. Schön, M. Kläui, and M. Weides, *Phys. Rev. B* **97**, 184420 (2018).

<sup>24</sup> I. Neudecker, G. Woltersdorf, B. Heinrich, T. Okuno, G. Gubbiotti, and C. Back, *J. Magn. Magn. Mat.* **307**, 148 (2006).

<sup>25</sup> S. S. Kalarickal, P. Krivosik, M. Wu, C. E. Patton, M. L. Schneider, P. Kabos, T. J. Silva, and J. P. Nibarger, *J. Appl. Phys.* **99**, 093909 (2006).

<sup>26</sup> Y.-C. Chen, D.-S. Hung, Y.-D. Yao, S.-F. Lee, H.-P. Ji, and C. Yu, *J. Appl. Phys.* **101**, 09C104 (2007).

<sup>27</sup> C. Dubs, O. Surzhenko, R. Linke, A. Danilewsky, U. Brückner, and J. Dellith, *J. Phys. D: Appl. Phys.* **50**, 204005 (2017).

<sup>28</sup> I. A. Golovchanskiy, V. V. Bolginov, N. N. Abramov, V. S. Stolyarov, A. B. Hamida, V. I. Chichkov, D. Roditchev, and V. V. Ryazanov, *J. Appl. Phys.* **120**, 163902 (2016).

<sup>29</sup> C. Kittel, *Phys. Rev.* **73**, 155 (1948).

<sup>30</sup> Y. V. Khivintsev, L. Reisman, J. Lovejoy, R. Adam, C. M. Schneider, R. E. Camley, and Z. J. Celinski, *J. Appl. Phys.* **108**, 023907 (2010).

<sup>31</sup> S. Klingler, A. V. Chumak, T. Mewes, B. Khodadadi, C. Mewes, C. Dubs, O. Surzhenko, B. Hillebrands, and A. Conca, *J. Phys. D: Appl. Phys.* **48**, 015001 (2015).

<sup>32</sup> J. O. Artman and S. H. Charap, *J. Appl. Phys.* **49**, 1587 (1978).

<sup>33</sup> M. Ramesh and P. E. Wigen, *J. Mag. Mag. Mater.* **74**, 123 (1988).

<sup>34</sup> I. S. Camara, S. Tacchi, L.-C. Garnier, M. Eddrief, F. Fortuna, G. Carlotti, and M. Marangolo, *J. Phys.: Condens. Matter* **29**, 465803 (2017).

<sup>35</sup> T. G. W. Blake, C.-C. Shir, Y.-Tu, and E. D. Torre, *IEEE Trans. Magn.* **18**, 985 (1982).

<sup>36</sup> F. Virot, L. Favre, R. Hayn, and M. D. Kuz'min, *J. Phys. D: Appl. Phys.* **45**, 405003 (2012).

<sup>37</sup> S. Lee, S. Grudichak, J. Sklenar, C. C. Tsai, M. Jang, Q. Yang, H. Zhang, and J. B. Ketterson, *J. Appl. Phys.* **120**, 033905 (2016).

<sup>38</sup> S. A. Manuilov, S. I. Khartsev, and A. M. Grishin, *J. Appl. Phys.* **106**, 123917 (2009).

<sup>39</sup> D. Stancil, *Theory of Magnetostatic Waves* (Springer-Verlag New York, Inc., 1993).

<sup>40</sup> A. A. Serga, A. V. Chumak, and B. Hillebrands, *J. Phys. D: Appl. Phys.* **43**, 264002 (2010).

<sup>41</sup> C. Kittel, *Phys. Rev.* **100**, 1295 (1958).

<sup>42</sup> M. H. Seavey and P. E. Tannenwald, *J. Appl. Phys.* **30**, S227 (1959).

<sup>43</sup> S. A. Bunyaev, V. O. Golub, O. Y. Salyuk, E. V. Tar takovskaya, N. M. Santos, A. A. Timopheev, N. A. Sobolev, A. A. Serga, A. V. Chumak, B. Hillebrands, et al., *Sci. Rep.* **5**, 18480 (2015).

<sup>44</sup> J. Smit and H. G. Beljers, *Philips Res. Rep.* **10**, 113 (1955).

<sup>45</sup> H. Suhl, *Phys. Rev.* **97**, 555 (1955).

<sup>46</sup> S. M. Rezende, J. A. S. Moura, F. M. de Aguiar, and W. H. Schreiner, *Phys. Rev. B* **49**, 15105 (1994).

<sup>47</sup> P. Hansen, *J. Appl. Phys.* **45**, 3638 (1974).

<sup>48</sup> B. M. Howe, S. Emori, H.-M. Jeon, T. M. Oxholm, J. G. Jones, K. Mahalingam, Y. Zhuang, N. X. Sun, and G. J. Brown, *IEEE Magnetics Letters* **6**, 3500504 (2015).

<sup>49</sup> B. Bhoi, B. Kim, Y. Kim, M.-K. Kim, J.-H. Lee, and S.-K. Kim, *J. Appl. Phys.* **123**, 203902 (2018).

<sup>50</sup> H. Maier-Flaig, S. Klingler, C. Dubs, O. Surzhenko, R. Gross, M. Weiler, H. Huebl, and S. T. B. Goennenwein, *Phys. Rev. B* **95**, 214423 (2017).

<sup>51</sup> C. Jooss, J. Albrecht, H. Kuhn, S. Leonhardt, and H. Kronmüller, *Rep. Prog. Phys.* **65**, 651 (2001).

<sup>52</sup> F. S. Wells, A. V. Pan, S. Wilson, I. A. Golovchanskiy, S. A. Fedoseev, and A. Rozenfeld, *Supercond. Sci. Technol.* **29**, 035014 (2016).

<sup>53</sup> F. S. Wells, A. V. Pan, I. A. Golovchanskiy, S. A. Fedoseev, and A. Rozenfeld, *Sci. Rep.* **7**, 40235 (2017).

<sup>54</sup> C. P. Bean, *Rev. Mod. Phys.* **36**, 31 (1964).

<sup>55</sup> W. T. Norris, *J. Phys. D: Appl. Phys.* **3**, 489 (1969).

<sup>56</sup> D.-X. Chen and R. B. Goldfarb, *J. Appl. Phys.* **66**, 2489 (1989).

<sup>57</sup> I. A. Golovchanskiy, A. V. Pan, O. V. Shcherbakova, and S. A. Fedoseev, *J. Appl. Phys.* **114**, 163910 (2013).

<sup>58</sup> M. Tinkham, *Phys. Rev. Lett.* **61**, 1658 (1988).

<sup>59</sup> I. A. Golovchanskiy, A. V. Pan, J. George, F. S. Wells, S. A. Fedoseev, and A. Rozenfeld, *Supercond. Sci. Technol.* **29**, 075002 (2016).

<sup>60</sup> K. Jeon, C. Ciccarelli, H. Kurebayashi, L. F. Cohen, X. Montiel, M. Eschrig, T. Wagner, S. Komori, A. Srivastava, J. W. A. Robinson, et al., *Phys. Rev. Appl.* **11**, 014061 (2019).

<sup>61</sup> D. F. Gibbons and V. G. Chirba, *Phys. Rev.* **110**, 770 (1958).

<sup>62</sup> K. Wang and R. R. Reeber, *Materials Science and Engi-*

neering **R23**, 101 (1998).

<sup>63</sup> S. Geller, G. P. Espinosa, and P. B. Crandall, Jr. *Appl. Cryst.* **2**, 86 (1969).

<sup>64</sup> R. sheng Liang and F. chao Liu, *Powder Diffraction* **14**, 2 (1999).

<sup>65</sup> H. J. Levinstein, E. M. Gyorgy, and R. C. LeCraw, *J. Appl. Phys.* **37**, 2197 (1966).

<sup>66</sup> A. M. Antyukhov, A. A. Sidorov, I. A. Ivanov, and A. V. Antonov, *Inorg. Mater.* (Translated from *Izv. Akad. Nauk SSSR, Neorg. Mater.*) **23**, 702 (1987).

<sup>67</sup> T. Y. Fan, D. J. Ripin, R. L. Aggarwal, J. R. Ochoa, B. Chann, M. Tilleman, and J. Spitzberg, *IEEE Journal of Selected Topics in Quantum Electronics* **13**, 448 (2007).